Air-breathing Mg-Cu/CuO fuel cell

R. Jayakrishnan[1]* , Aruna Raj[1], Akhil M. Anand[1], P C Harikrishnan[1] and Athira Ayyappan[1]

*Correspondence:
rjk@keralauniversity.ac.in

[1] Modular Thin Film Fab
Lab, Department of Physics,
University of Kerala,
Thiruvananthapuram 695581,
India

Abstract

Magnesium fuel cells deliver higher electrical power output than lithium-ion batteries and have the potential to become an economically attractive alternative power source for domestic purposes. In place of noble metals in the air cathode of Mg fuel cells, we investigate the use of an integrated structure of a catalyst and current collector composed of a Cu/CuO hetero-structure. For a single cell, comprising of electrodes of dimension 3 cm × 1.5 cm with aqueous NaCl as the electrolyte, the Mg- Cu/CuO-based fuel cell shows an open-circuit voltage of 0.7 V and discharge current drain rate of 0.45 mA/s. A power density of 8.75 μWcm^{-2} is obtained with a CuO-based cathode when 1 M NaCl electrolyte is used. Relative to the magnesium-carbon-based fuel cell, the Mg-Cu/CuO fuel cell shows improved stability of the anode and cathode materials and extended operational time.

Keywords: Magnesium, Cupric oxide, Salt water, Fuel cell

Introduction

The advent of climate change has pushed researchers to pursue the development of green energy devices that are economically viable and environmentally sustainable. The lookout for batteries that are potentially on a robust supply chain, more sustainable to engineer, and cost-effective than state-of-the-art lithium-ion batteries has recently found a new harbinger in Mg-based batteries [1–4]. Magnesium metal is an attractive anode material owing to its high abundance in the earth's crust [5]. Technologically it is lucrative because of its volumetric capacity of 3833 mAh cm^{-3}, gravimetric capacity of 2205 mAh g^{-1}, and a low redox potential of (−2.37 V vs. SHE) [6]. The divalent character of Mg^{2+} in oxidation offers two electrons per metal (Mg) compared to only one electron in the case of alkali metals, such as Li and Na. Hence, the potential to realize a higher energy density relative to lithium-based cells makes the material investigation worthy [7–9].

Theoretically, magnesium-ion batteries function very similar to lithium-ion batteries [3]. Magnesium ions are transported between a negative anode and a positive cathode, made of a metal-oxide material [10]. This allows the electrons to move around an external circuit and do work. But as magnesium is a small ion carrying a lot of electric charge, it gets tangled in unwanted interactions with surrounding materials. Transfer of magnesium from the electrolyte to solid electrodes requires excess energy and often results in "parasitic" reactions that compete with the process of storing charge, which

limits the lifetime of the batteries [8]. Additionally, the motion of magnesium through all materials is more sluggish than lithium [6]. Because of this, charge transfer rates are limited. Magnesium air fuel cells are at an early stage of development and are recognized for their higher energy density [11]. For the Mg-air fuel cell technology, there is a magnesium anode, a gas diffusion (air) cathode layer, and an electrolyte. The air cathode layer has typically four components: (a) a membrane that allows oxygen from the air to enter the cell and facilitates the oxidation–reduction reaction between the magnesium and the electrolyte, (b) a gas diffusion layer, (c) a catalyst layer, and (d) current collector layer [11].

Noble metals are usually used as the catalyst layer for the oxygen reduction reaction (ORR), on the surface of the gas diffusion layer near the electrolyte. Anode corrosion and low coulombic efficiency of the Mg-air fuel cell are ascribed to the over-potential of the air cathode. The use of Pt and Pt-based alloys as catalysts has been investigated for the ORR previously [12–19]. Catalysts based on Pd, Ag, Au, and non-Pt alloys which demonstrated lower and higher activity respectively relative to Pt were also reported [20–24]. The use of carbon and modified carbon yielded much higher over-potential and improved stability [25–30]. The use of transition metal oxides yielded lower electro-catalytic activity [31, 32]. The use of complexes of oxides with r-GO yielded high activity comparable to Pt [33, 34]. The use of nitrogen-containing metallic complexes showed high activity comparable to Pt/C [35, 36]. Thus, an improvement in the air cathode is an area of intense research.

Nobel metals like Pd, Cu, and Ag have high oxygen reduction activity and can be used as ORR catalysts. The abundance and lower cost of Cu relative to Pt make it a suitable candidate for ORR. In the present work, we attempt the use of an integrated structure comprising of the catalyst and current collector layers by the use of a semiconducting layer of CuO grown over Cu substrate in an Mg-NaCl-based fuel cell for improving the kinetics of the ORR. Since the catalytic production of hydrogen from NaCl solution is a low-cost, high-efficiency process, we explored its potential as the electrolyte material in our fuel cell structure. We compare the performance of the integrated cathode structure with that of a standard carbon cathode to quantify the performance of the fuel cell. This work is a harbinger in the area of air-breathing Mg-Cu/Cuo fuel cells.

Methods

Oxidation of copper metal in KOH solution was used for the growth of CuO. Details of the method of preparation and detailed characterization of the grown CuO have been reported previously [37]. Cu/CuO sheets of dimension 3 cm × 1.5 cm were used as the cathode. Graphitic carbon cloth was purchased and cut to the same dimensions of 3 cm × 1.5 cm for use as a cathode to compare the performance of the Cu/CuO cathode. The crystal structure of various materials used for the study was identified using X-ray diffraction studies. Field emission scanning electron microscopy was carried out to characterize the surface morphology of the electrodes used. EDAX was carried out for the elemental analysis of the materials. XPS studies were conducted on the Mg electrodes to identify the presence of impurities like oxides and hydroxides. To identify structural changes as a result of oxidation, Raman analysis was conducted on the electrodes before and after the operation of the fuel cell. Figure 1 represents a schematic of the fuel cell
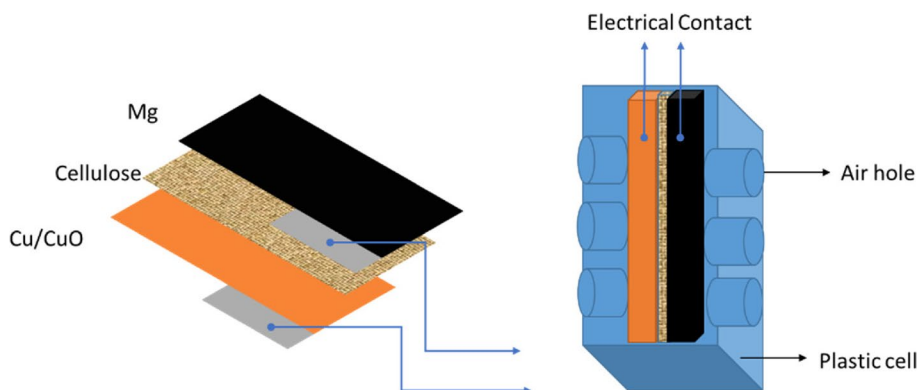
Fig. 1 Schematic of the fuel cell designed and experimented herein

designed and used in our studies. The two electrodes separated by the electrolyte-soaked cellulose were placed inside a grooved plastic container with holes on the opposite sides to permit the flow of air. As shown in Fig. 1, the electrical connections were taken from one side of the electrode. Mg metal strips of 3 cm × 1.5 cm × 1 cm were used as the anode for all of the studies. A strip of cellulose soaked in 1 M NaCl solution in distilled water was used to separate the two electrodes. Electrical testing of the fuel cell under short-circuit mode was conducted using a two-channel source measuring unit. Using an electrochemical workstation, the characteristics of the fuel cell were studied using the three-electrode configuration.

Results and discussion

Figure 2a shows the X-ray diffraction (XRD) patterns of the graphite carbon electrode. The spectra show the crystalline nature of the sample with preferential orientation along the (002) plane. Other planes (101), (102), and (004) could also be indexed. The inter-planar spacing (d_{002}) was calculated using Bragg's relation (1) and was found to be ~ 0.338 nm [38]. The value is in close agreement with the correct value for the inter-planar distance of the graphite which is 0.335 nm.

$$d_{(002)} = \frac{\lambda}{2} \sin(\theta_{(002)}) \tag{1}$$

The degree of graphitization (g) was determined to be 3.13 using the Franklin equation as (2)

$$g = \frac{(0.3440 - d_{(002)})}{(0.3440 - 0.3354)} \times 100\% \tag{2}$$

where 0.3440 and 0.3354 are the carbon layer spacing in nano-meters for the original carbonaceous materials and the ideal graphite crystal, respectively [39]. For the carbon layer, the average stacking height (L_c) was evaluated using the Scherer formula (3)
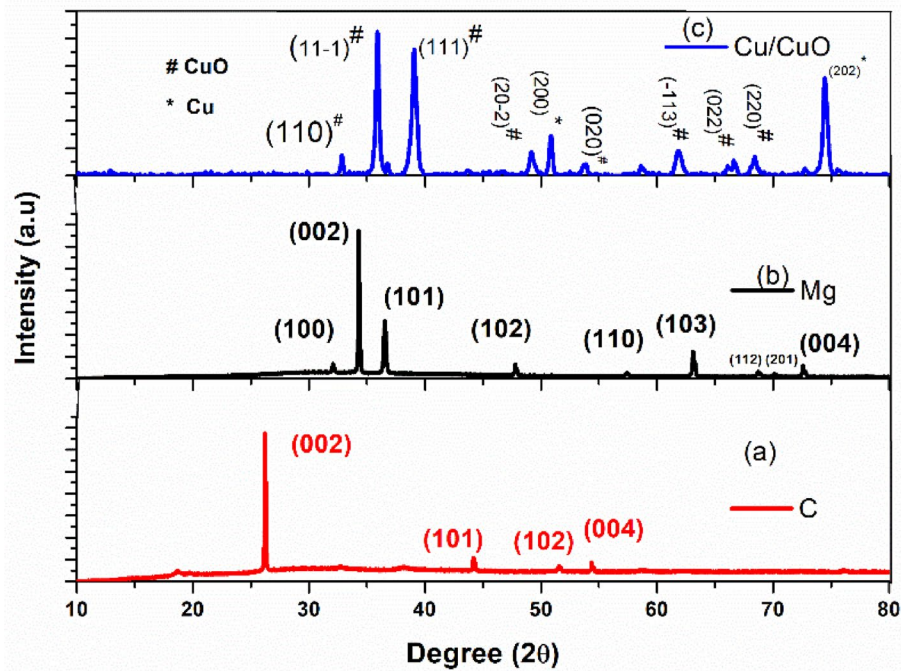
Fig. 2 XRD spectra for (**a**) carbon electrode, (**b**) Mg metal, and (**c**) Cu/CuO

$$L_c = \frac{k\lambda}{\beta_{(002)} \cos\theta_{(002)}} \tag{3}$$

where $k = 0.94$ is the Scherer parameter, $\beta_{(002)}$ represents the full width at half maximum for the diffraction peak corresponding to the (002) plane, and $\theta_{(002)}$ is the Bragg angle corresponding to the diffraction peak [40]. The stacking height was obtained as ~1.35 nm for our carbon electrode. For a parallel stacked graphitic carbon, the stacking height is related to the lattice spacing by the relation

$$L_{(002)} = (N-1)d_{(002)} \tag{4}$$

where N is the number of parallel layers in a stack [41]. This was calculated to be ~4.9 in our sample.

The average number of carbon atoms per aromatic lamellae is by the relation

$$n = 0.32N^2 \tag{5}$$

using which we estimate $n = 7.9$ [41].

Figure 2(b) shows the XRD patterns of the metallic Mg plate. Crystalline planes along the (100), (002), (101), (102), (110), (103), (112), (201), and (440) planes could be indexed. The inter-planar spacing (d_{002}) was calculated using Bragg's relation (1) and was found to be ~0.261 nm. The average crystallite size (L_a) was evaluated using the Scherer formula (6)

$$L_a = \frac{k_1\lambda}{\beta_{(100)} \cos\theta_{(100)}} \tag{6}$$

where $k = 1.84$ is the Scherer parameter, $\beta_{(100)}$ represents the full width at half maximum for the diffraction peak corresponding to the (100) plane, and $\theta_{(100)}$ is the Bragg angle corresponding to the diffraction peak [40]. The average crystallite size was found to be ~ 1.4 nm. The stacking height L_c using Eq. (3) was found to be ~ 1 nm. Magnesium has a hexagonal closed-packed crystal structure belonging to the $P6_3$/mmc space group.

Figure 2(c) shows the XRD patterns of the CuO thin film layer grown over flexible Cu foils using a self-assembly process detailed previously by us [37]. The spectra show that the grown films are polycrystalline in nature. The growth planes were indexed, and it is found that the films have preferential orientation along the $(11\bar{1})$ plane corresponding to the $2\theta = 35.56^0$ cubic phase of CuO. Significant planes along the (110), (111), $(2\,02)$, (020), $(\bar{1}\,13)$, (022), and (220) were also evident from the spectra. XRD peaks corresponding to the Cu substrate were also identified from the spectra.

Figure 3 represents the field emission scanning electron microscopy (FESEM) images for the materials used for the fuel cell. Figure 3a on the left represents the FESEM surface morphology of the carbon electrode material. At a scale of 2 μm, the flat layered structure is evident from the figure and complements the interpretations of the XRD data analysis. The FESEM image on the right represents a magnified image at a scale of 100 nm. At this scale, the presence of floret microstructure is evident. The lateral dimension of the floret structures was estimated to be ~ 38 nm. The floret structure appears to be delineated from each other by the presence of a cracked lamella which are homogenously distributed throughout the surface. Figure 3b represents the FESEM image of the Mg electrode material. The surface morphology at a scale of 2 μm appears to be consisting of a cracked lamella with non-uniformly distributed agglomerated matter of no definite shape spread over. The FESEM image on the right representing the magnified image of Mg surface at a scale of 100 nm shows the same morphology as that of carbon but with a finer-sized spherical structure distributed uniformly. The lateral dimension of the spherical structures was estimated to be ~ 70 nm. Figure 3c represents the FESEM image of the cellulose membrane material used for in the cell. At a scale of 100 μm, the presence of layered strands in the form of a mesh structure is clearly recognized. The magnified image on the right at a scale of 2 μm shows the thickness of each strand to be ~ 16 μm. In general, from Fig. 3, we can conclude that all three materials appear to have a porous structure which will eventually aid in the flow of air required for fuel cell application. It would also be essential from the perspective of loading of electrolyte within these porous structures enabling the transport of charge carriers.

Table 1 presents the summary of the energy dispersive X-ray analysis (EDAX) measurements done on the carbon electrode and the Mg electrode materials taken for this work. The incidence of oxygen is unfavorable to the performance of carbon electrodes in organic electrolytes. We assume that the oxygen identified by EDAX is primarily surface oxygen in our graphite carbon electrode. For Mg electrode, the presence of oxygen is required to verify if oxidation of the metal had occurred.

Figure 4 represents the results of the XPS analysis of the Mg electrode used in this work. The scan shows the binding energy peaks corresponding to Mg (1 s) at 1303.05 eV, two species of C (1 s) with binding energies at 288.25 eV and 283.1 eV, an oxygen (1 s) specie with binding energies at 530.4 eV and a sodium (1 s) specie with binding energy of 1070.55 eV. The results of the XPS analysis show that oxidation of
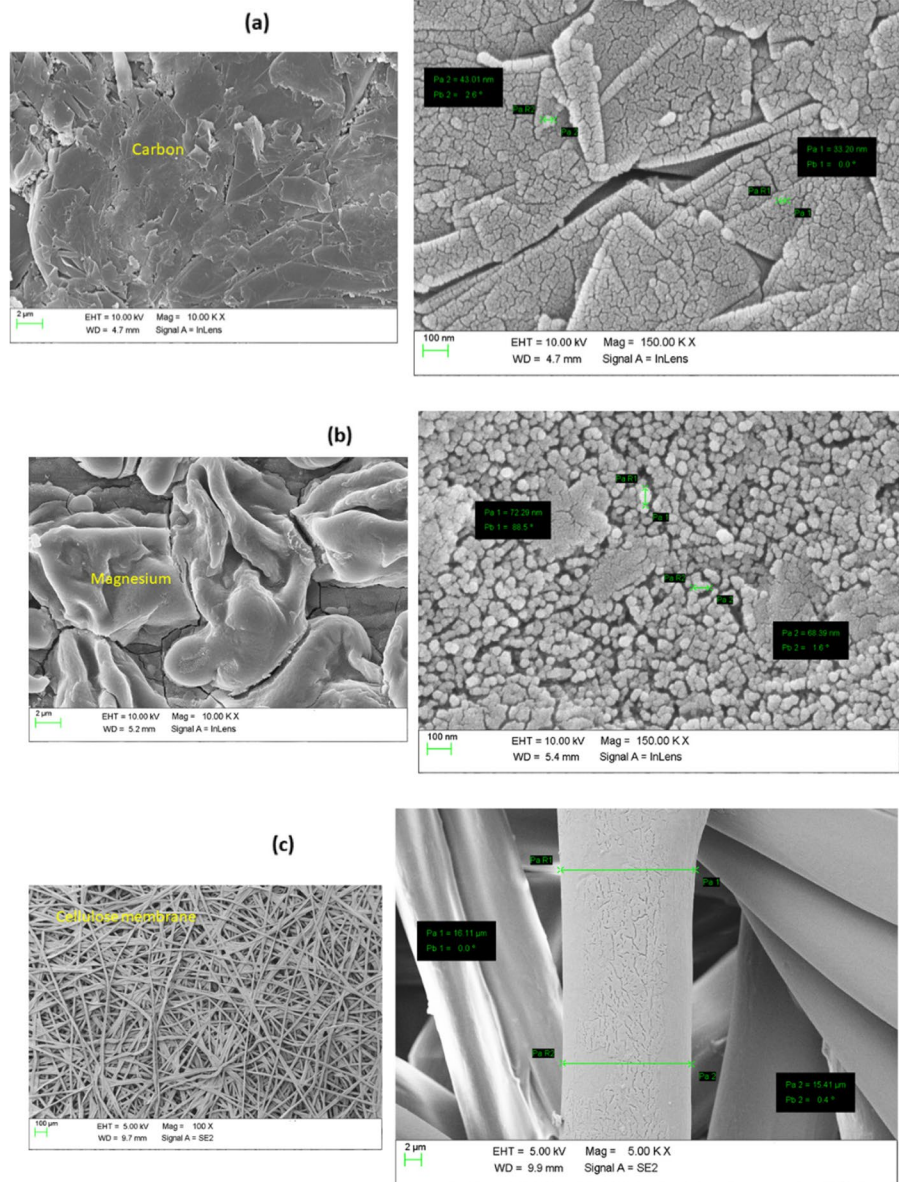
Jayakrishnan *et al. Journal of Engineering and Applied Science*   (2024) 71:78

Page 6 of 13

Fig. 3 FESEM images of **a** carbon, **b** magnesium, and **c** cellulose

Table 1 Elemental composition from EDX measurement

Sample	Elements	Wt %	Atom %
Carbon	Carbon	72.41	77.76
	Oxygen	27.59	22.24
Magnesium	Magnesium	36.15	25.55
	Oxygen	47.17	50.64
	Carbon	16.63	23.78
	Sodium	0.04	0.03
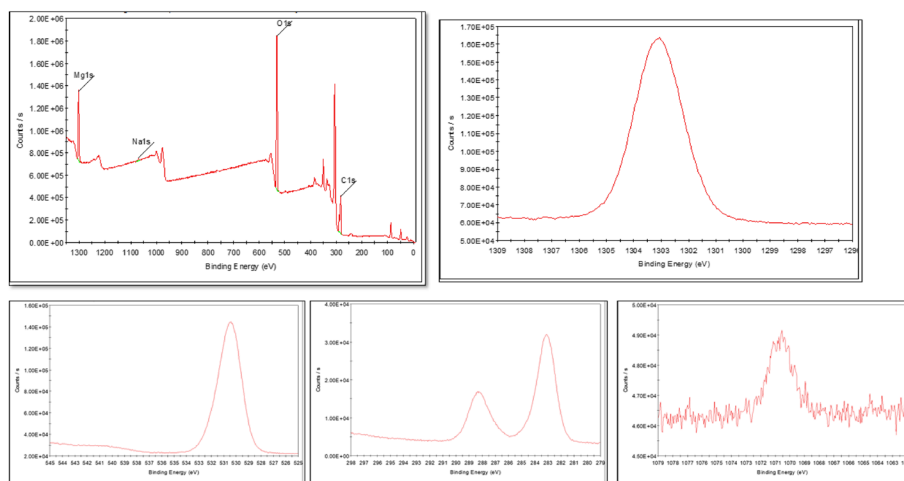
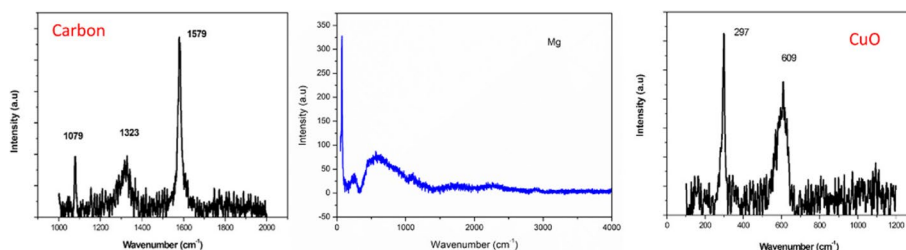**Fig. 4** XPS results for the Mg electrode

Fig. 5 Raman spectra for carbon, Mg, and Cu/CuO electrodes

Mg may not have occurred as there is no shift in the binding energy of Mg. The presence of metal carbide is identified by the presence of a peak at 283.1 eV and O−C=O/CO_3 is identified based on the peak at 288.25 eV.

Figure 5 represents the Raman spectra for the electrode materials used. For the carbon electrode, the Raman spectra show that the carbon material used exhibits a very high degree of three-dimensional ordering confirming it to be a highly oriented pyrolytic graphite exhibiting the G band at 1579 cm^{-1} [42]. The G band is a characteristic peak of graphene-related materials and is used to quantify the response of materials and devices based on graphene to external perturbations. The G band is associated with the doubly degenerate phonon mode corresponding to the E_{2g} symmetry. Single crystal graphite belongs to the D46h symmetry group and shows vibrational modes of the types 2 E2g, 2B2g, E1u, and A2u. The peak at 1579 cm^{-1} (G band) with very strong relative intensity indicates the vibration of E2g mode. The peak at 1323 cm^{-1} (D band) corresponds to the A1g mode of vibration. The peak at 1079 cm^{-1} corresponds to the stretching vibration of the C−C bonds [43]. It is well known that a change in polarizability during molecular vibrations results in the generation of Raman spectra. For the metal Mg, there occurs no change in polarizability which is evidenced by the absence of any Raman peak in the spectra recorded. The Raman spectra for the CuO grown
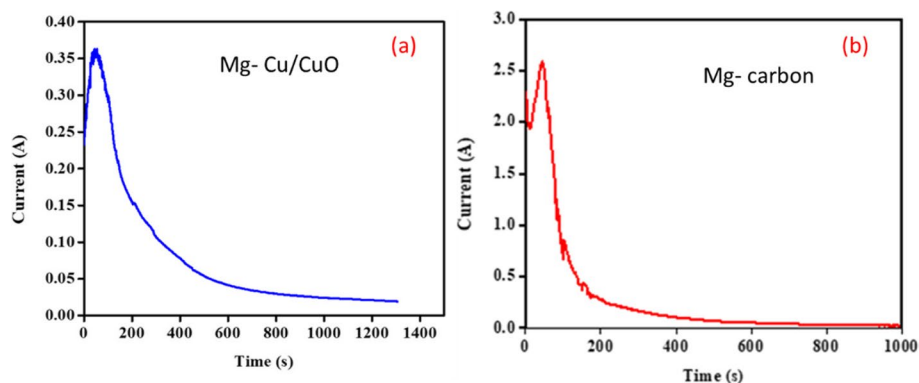
Fig. 6 Short-circuit studies conducted by the application of constant voltage of 2 V with 1.0 M NaCl injected into the cathode air stream for **a** Mg-CuO cell and **b** Mg-carbon cell
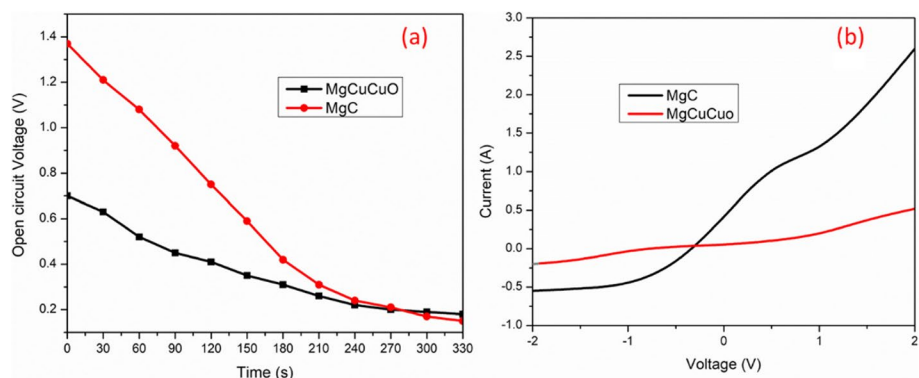

Fig. 7 For the Mg-carbon cell and Mg-Cu/CuO cell **a** temporal dependence of open-circuit voltage and **b** current–voltage (CV) characteristics

over Cu substrate show two peaks one at 297 cm^{-1} and another at 609 cm^{-1} which are the characteristic Raman peak for CuO [44].

Figure 6 shows the results of the test conducted on the fuel cells under short-circuit conditions, where the current was monitored during the discharge cycle. Figure 6a represents the results for the Mg-CuO fuel cell and Fig. 6b that of the Mg-carbon fuel cell. It is evident that the Mg-carbon cell exhibits a relatively quick discharge compared to the Mg-Cu/CuO fuel cell. The Mg-carbon cell exhibited an exponential discharge where the current decreased from 2.55 A to 0.25 A in ~ 200 s after which a discharge plateau was evident. In the case of the Mg-Cu/CuO fuel cell, the current decreased from 0.36 A to 0.04 A in ~ 700 s. Thus, the discharge current drain was 11.5 mA/s for the Mg-carbon cell and 0.45 mA/s for the Mg-Cu/CuO fuel cell.

Figure 7a represents the rate of change in open-circuit voltage across the fuel cells when they are drained by a load of 200 mW. The results show that the rate of decrease of open-circuit voltage is slower for the Mg-Cu/Cuo fuel cell relative to the Mg-C fuel cell. Figure 7b represents the current–voltage measurement conducted for the fuel cells using a source measurement unit in the two-probe mode. A voltage scan from − 2 to + 2 V was carried out across the two electrodes of the cells. The measurement shows that the Mg-C cells have higher conductivity relative to the Mg-CuO

cells. Thus, we could conclude that the larger discharge current drain exhibited by the Mg-C cells was because of its higher conductivity.

In order to evaluate the performance of the CuO anode under fuel cell operation, cyclic voltammogram for the anode were obtained by stopping the fuel cell operation and subjecting the anode to CV measurements. Figure 8a represents the CV measurements for the Cu/CuO electrode carried out at a sweep rate of 100 mV/s by scanning the potential from −0.5 to 1 V. The shape of the voltammogram indicates that a non-reversible electron transfer is occurring during the reverse scans from 1 to −0.5 V. The area of the voltammogram decreased after subsequent cycles without a change in the shape of the absorption/desorption peaks. The distinct shifts to higher potential in the voltammogram with each subsequent scan cycle show that the system is kinetically limited. To verify this, scans were conducted by varying the sweep rates as shown in Fig. 8b. When the scan rates are increased beyond 250 mV/s, no peak-to-peak separation is observed representing that the electrolyte ions and the active species in the electrode fail to interact and no electron transfer takes place. Also, the area under the voltammogram decreases as the scan rates are increased demonstrating that the power per active surface area of the electrode is decreasing. The presence of the reduction peak in the voltammetry curves indicates the capacitive performance of the electrode under the potential range. Our results show that the Cu/CuO electrode undergoes reduction between the 0.6–0.8 V (vs SHE) range. Electrochemical active surface area (ECSA) measurements were conducted using the area under the voltammetry curve using the relation:

$$ESCA\,(\mathrm{m^2g^{-1}}) = \frac{\frac{S_H}{V}}{10 \times 0.21\,(\mathrm{mCcm^{-2}}) \times M} \tag{7}$$

where S_H is the area under the curves (A V), V is the sweep rate (V s^{-1}), the conversion value for the desorption of a hydrogen monolayer is used as 0.21 mC cm^{-2}, and M (g) is the mass of the electrode material [45]. The Mg-Cu/CuO fuel cell was estimated to have a lower value for ESCA (18 m^{2}g^{-1}) relative to the Mg-C fuel cell ESCA (38 m^{2}g^{-1}). To compare the degradation of ECSA with each operation cycle, the percentage change of catalysts is normalized with respect to its initial state value of ECSA. Figure 9 shows the variation of % ESCA with cycling, exhibiting a reducing trend with each cycle.
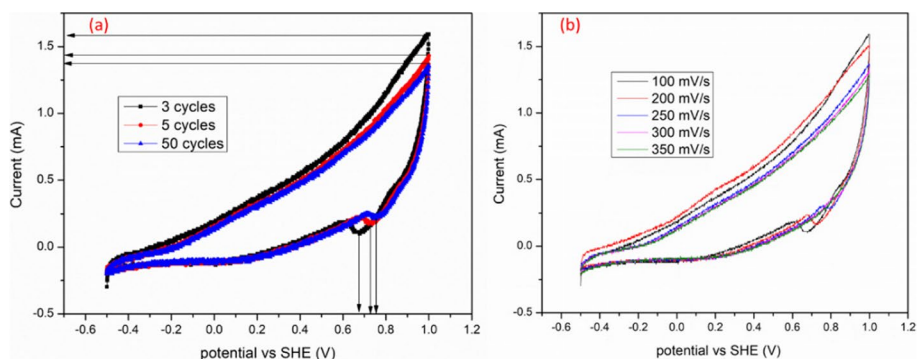

Fig. 8 Cyclic voltammetry curves of Cu/CuO **a** between − 0.5 and 1.0 V with a scan rate of 100 mV s^{-1} and **b** between − 0.5 and 1 V with the scan rate varied from 100 mV/s to 350 mV/s

Jayakrishnan *et al. Journal of Engineering and Applied Science* (2024) 71:78
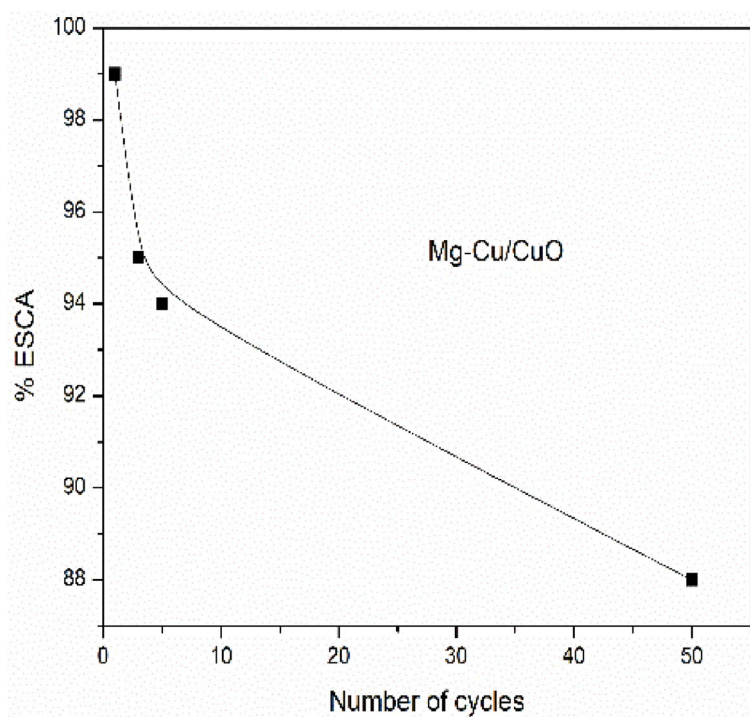
Page 10 of 13

Fig. 9 Variation of % ESCA with each scan cycle

Based on the ESCA calculation, we conclude that an excess supply of ionomer content on the catalyst may wrap the catalyst and block the catalyst sites leading to a decrease in mass transport. This would be manifested in the form of reduced current intensity from the fuel cell as evidenced in Fig. 6. The overall reaction of the fuel cell during its operation is

$$2Mg + 6NaCl + 6H2O \rightarrow 2MgCl3 + 6NaOH + 3H_2 \tag{8}$$
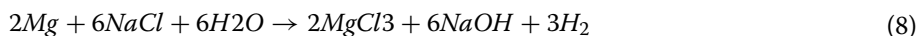
Polarization studies could be used to complement the observed ECSA decrease. Figure 10 shows the polarization curve for the Mg-Cu/CuO and Mg-C fuel cell, where the test electrode potential was increased in the anodic direction, until the applied potential, reached the preselected maximum magnitude. For the Cu/CuO electrode, the polarization curve exhibits four distinct regions with the graph showing that the mass transport resistance is the most limiting process in this fuel cell device architecture. The effect of the activation over-potential required to drive the electrochemical reaction is evident in the low current density regions. For the "C" electrode in the Mg-C fuel cell, the polarization curve predominantly exhibits effects of ohmic resistance and also is showing that the mass transport resistance is the most limiting process.

Conclusions

We have been able to engineer an air-breathing Mg-Cu/CuO fuel cell consisting of an integrated structure of the catalyst and current collector using Cu/CuO structure for this purpose. The fuel cell has been demonstrated in this report using saline water as the working electrolyte. Under short-circuit conditions, the Mg-Cu/CuO fuel cell delivers a maximum
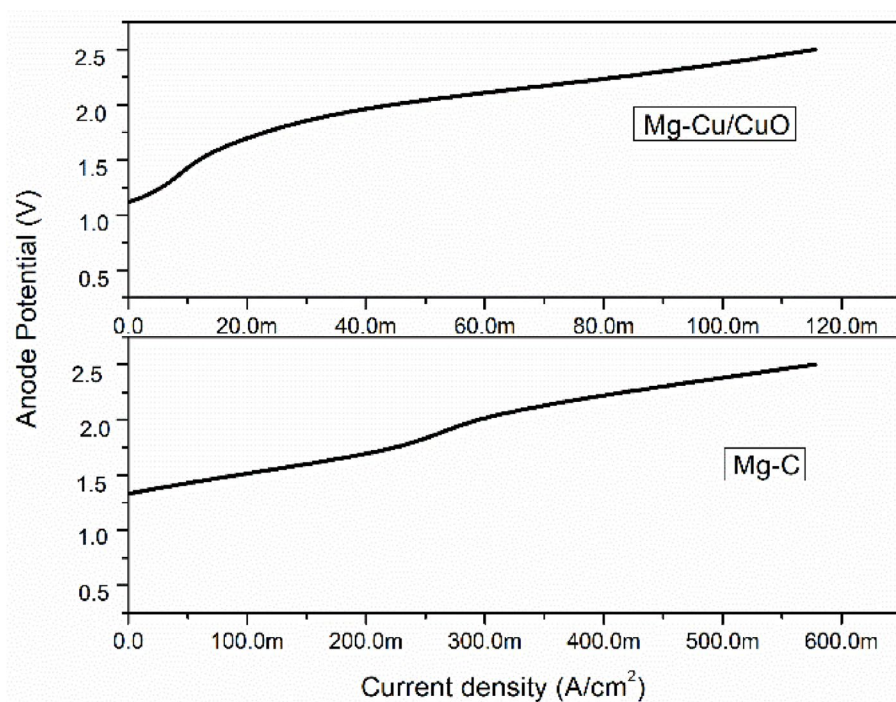
Fig. 10 Polarization curves for the "Cu/CuO" and "C" anodes respectively at a sweep rate of 10 mV/s

current of 0.35 A, which is lower than that of the 2.55 A achieved by the Mg-C fuel cell under similar test conditions. The maximum open-circuit voltage of the Mg-Cu/CuO fuel cell was 0.70 V relative to 1.37 V achieved by the Mg-C fuel cell. A power density of ∼ 8 μWcm^{-2} was delivered when operated with 1 M NaCl electrolyte which was much lower than that of the 1.16 Wcm^{-2} obtained from the Mg-C fuel cell under the same test conditions. Relative to the Mg-C fuel cell, the Mg-Cu/CuO fuel cell exhibits a lower rate of drain of discharge current indicating that they are operationally more stable than the former. For the Mg-C cell, the carbon cathode could not be reused as it disintegrated after 3 h of operation. For the Mg-Cu/CuO cell, the Cu/CuO electrode could be reused but delivered lower power density on subsequent trails. Based on ESCA, we conclude that an excess supply of ionomer content on the catalyst may be wrapping the catalyst and blocking the catalyst sites which leads to a decrease in the operational efficiency of the Mg-Cu/CuO fuel cell. Polarization studies identified that mass transport resistance was the most limiting process for both of the device architectures. Our effort to identify an alternative catalyst in place of the exquisite Pt and Ag for the air cathode system in the form of an integrated structure of the catalyst and current collector has yielded promising results. It may be worth applying more efforts in this direction to develop Cu/CuO system for the Mg-air fuel cell.

Abbreviations

EDAX	Energy dispersive X-ray analysis
ORR	Oxygen reduction reaction
CV	Current voltage
SHE	Standard hydrogen electrode
FESEM	Field emission scanning electron microscopy
XRD	X-ray diffraction
ESCA	Electrochemical active surface area

Availability of data and materials
Data will be available upon reasonable request to the corresponding author.

Declarations

Competing interests
The authors declare that they have no competing interests.

References
1. Wei C, Tan L, Zhang Y, Xi B, Xiong S, Feng J, Qian Y (2022) Energy Storage Materials 48:447–457
2. Wei C, Tan L, Zhang Y, Wang Z, Feng J, Qian Y (2022) Energy Storage Materials 52:299–319
3. Yasuaki Kohama, Michiru Sakamoto, Toshihiko Abe (2015) US Patent No. US9461305B2
4. Medeiros MG, Bessette RR, Dischert D, Cichon J (2001) US Navy Patent No. 6228527
5. Bella F, De Luca S, Fagiolari L, Versaci D, Amici J (2021) Carlotta Francia and Silvia Bodoardo. Nanomaterials 11(3):810. https://doi.org/10.3390/nano11030810
6. Zhang J, Guan X, Lv R, Wang D, Liu P, Luo J (2020) Energy Storage Materials 26:408–413
7. Naga Mahesh K, Balaji R, Dhathathreyan KS (2015) Ionics 21:2603–2607. https://doi.org/10.1007/s11581-015-1434-y
8. Bella F, De Luca S, Fagiolari L, Versaci D, Amici J, Francia C, Bodoardo S (2021) Nanomaterials (Basel) 11(3):810
9. Zhang Y, Geng H, Wei W, Ma J, Chen L, Li CC (2019) Energy Storage Materials 20:118–138
10. Li D, Yuan Y, Liu J, Fichtner M, Pan F (2020) Journal of Magnesium and Alloys 8(4):963–979
11. Zhang T, Tao Z, Chen J (2014) Mater Horiz 1:196–206
12. Perez J, Gonzalez ER, Ticianelli EA (1998) Electrochim Acta 44:1329–1339
13. Lima FHB, Salgado JRC, Gonzalez ER, Ticianelli EA (2007) J Electrochem Soc 154:A369–A375
14. D. Wang, Y. Yu, H. L. Xin, R. Hovden, P. Ercius, J. A. Mundy, H. Chen, J. H. Richard, D. A. Muller, F. J. DiSalvo and H. D. Abruna, ˜ Nano Lett., 2012, 12, 5230–5238.
15. Wang D, Xin HL, Hovden R, Wang H, Yu Y, Muller DA, DiSalvo FJ, Abruna HD (2013) ˜ Nat. Mater 12:81–87
16. H. Chen, D. Wang, Y. Yu, K. A. Newton, D. A. Muller, H. Abruna and F. J. DiSalvo, ˜ J. Am. Chem. Soc., 2012, 134, 18453–18459.
17. Lima FHB, Ticianelli EA (2004) Electrochim Acta 49:4091–4099
18. Oezaslan M, Hasche F, Strasser P (2012) J Electrochem Soc 159:B444–B454
19. Jiang LH, Hsu A, Chu D, Chen RR (2009) J Electroanal Chem 629:87–93
20. Yang YF, Zhou YH, Cha CS (1995) Electrochim Acta 40:2579–2586
21. Jiang L, Hsu A, Chu D, Chen R (2010) Electrochim Acta 55:4506–4511
22. Schmidt TJ, Stamenkovic V, Arenz M, Markovic NM, Ross PN (2002) Electrochim Acta 47:3765–3776
23. Yang DS, Bhattacharjya D, Inamdar S, Park J, Yu JS (2012) J Am Chem Soc 134:16127–16130
24. Yang W, Fellinger TP, Antonietti M (2011) J Am Chem Soc 133:206–209
25. Wang H, Maiyalagan T, Wang X (2012) ACS Catal 2:781–794
26. Gong K, Du F, Xia Z, Durstock M, Dai L (2009) Science 323:760–764
27. Geng DS, Chen Y, Chen YG, Li YL, Li RY, Sun XL, Ye SY, Knights S (2011) Energy Environ Sci 4:760–764
28. Lai L, Potts JR, Zhan D, Wang L, Poh CK, Tang C, Gong H, Shen Z, Lin J, Ruoff RS (2012) Energy Environ Sci 5:7936–7942
29. Cheng FY, Su Y, Liang J, Tao ZL, Chen J (2010) Chem Mater 22:898–905
30. Gorlin Y, Jaramillo TF (2010) J Am Chem Soc 132:13612–13614
31. Suntivich J, Gasteiger HA, Yabuuchi N, Nakanishi H, Goodenough JB, Horn YS (2011) Nat Chem 3:546–550
32. Wu ZS, Yang SB, Sun Y, Parvez K, Feng XL, Mullen K (2012) J Am Chem Soc 134:9082–9085
33. Liang YY, Li YG, Wang HL, Zhou JG, Wang J, Regier T, Dai HJ (2011) Nat Mater 10:780–786
34. Liang Y, Wang H, Zhou J, Li Y, Wang J, Regier T, Dai H (2012) J Am Chem Soc 134:3517–3523
35. Liu RL, von Malotki C, Arnold L, Koshino N, Higashimura H, Baumgarten M, Mullen K (2011) J Am Chem Soc 133:10372–10375
36. Guo JS, Li HX, He H, Chu D, Chen RR (2011) J Phys Chem C 115:8494–8502
37. R Jayakrishnan, Akhil M Anand and Varun G Nair, Materials Research express 6,1250d9 (2020)
38. Qiu T, Yang J-G, Bai X-J, Wang Y-L (2019) RSC Adv 9:12737–12746
39. I. Came´an, P. Lavela, J. L. Tirado and A. B. Garc´ıa, Fuel, 2010, 89, 986–991.

40. Scherrer P (1918) Math-Phys Kl 2:98
41. Manoj B, Kunjomana AG (2012) Int J Electrochem Sci 7:3127–3134
42. Rizzarelli P, Rapisarda M, Perna S, Mirabella EF, La Carta S (2016) PuglisiC, Determination of polyethylene in bio-degradable polymer blends and in compostable carrier bags by Py-GC/MS and TGA. J Anal Appl Pyrolysis 117:72–81
43. Li T, Ichimura M (2021) Fabrication of Transparent Mg(OH)2 Thin Films by Drop-Dry Deposition. Materials 14(4):724
44. Guha S (1991) Dale Peebles and J Terence Wieting. Bull Mater Sci 14(3):539–543
45. Li Y, Xiong D, Liu Y, Liu M, Liu J, Liang C, Li C, Jun Xu (2019) Nanotechnol Rev 8(1):493–502. https://doi.org/10.1515/ntrev-2019-0044

Publisher's Note